Materials Science in Semiconductor Processing 202 (2026) 110128

Contents lists available at ScienceDirect

Materials Science in Semiconductor Processing

journal homepage: www.elsevier.com/locate/mssp

Novel Z-scheme AgI@$PbBiO_2Br$ heterojunction for efficient photodegradation of organic pollutants and bacteria inactivation: DFT simulation, explore active radicals, and mechanism insight

Ahsan Nazir [a,b,c,*], Ameena Tur Rasool [d,**], Chuntao Chen [a], Otabek Mukhitdinov [e], Doniyor Jumanazarov [f], Dongping Sun [a,***]

[a] Institute of Chemicobiology and Functional Materials, School of Chemistry and Chemical Engineering, Nanjing University of Science and Technology, Nanjing, Jiangsu, 210094, China
[b] School of Materials Science and Engineering, Nanjing University of Science and Technology, Nanjing, Jiangsu, 210094, China
[c] Low Dimensional Materials Research Center at Khazar University, AZ1096, Baku, Azerbaijan
[d] State Key Laboratory of Pharmaceutical Biotechnology, Medical School, Nanjing University, Nanjing, Jiangsu, 210093, China
[e] Kimyo International University in Tashkent, Shota Rustaveli str. 156, Tashkent, 100121, Uzbekistan
[f] Urgench State University, Kh. Alimdjan str. 14, Urgench, 220100, Uzbekistan

ARTICLE INFO

Keywords:
AgI@$PbBiO_2Br$ heterojunction
Pollutants degradation
Bacteria inactivation
DFT simulation
Mechanism analysis

ABSTRACT

In this study, novel Z-scheme AgI@$PbBiO_2Br$ heterojunctions were prepared using a simple in situ precipitation approach to effectively degrade organic pollutants and inactivate gram-negative Escherichia coli (E. coli) and gram-positive Staphylococcus aureus (S. aureus) bacteria when exposed to visible light. The prepared materials were comprehensively evaluated using several analytical procedures. The 20 %-AgI@$PbBiO_2Br$ presented the best photocatalytic performance of all the catalysts prepared. The rhodamine B (RhB) molecules were significantly reduced within 70 min (98.72 %), showing a much higher degradation efficiency than bare AgI (73.58 %) and $PbBiO_2Br$ (46.77 %) under the same conditions. The degradation of methyl orange (MO), neutral red (NR), and tetracycline (TC) by 20 %-AgI@$PbBiO_2Br$ was also examined, resulting in nearly total elimination of MO, NR, and TC pollutants, respectively. In addition, the antibacterial efficacy of 20 %-AgI@$PbBiO_2Br$ against E. coli and S. aureus reaches about 99.99 %. The improved photodegradation efficacy of AgI@$PbBiO_2Br$ is owing to the construction of a heterojunction between AgI and $PbBiO_2Br$, which increases effective charge separation and visible light absorption, thus enabling the decomposition of pollutants. Cycling experiments confirmed the stability and reusability of the material, demonstrating exceptional photocatalytic durability. The photocatalytic mechanism was thoroughly examined by reactive species capture assays and ESR analysis, confirming that holes and superoxide radicals are crucial in the photodegradation system. Additionally, the density functional theory (DFT) simulations and liquid chromatography-mass spectrometry (LC-MS) helped to clarify the susceptible active sites and possible degradation pathways of RhB. Overall, this work underlines the considerable ability of AgI@$PbBiO_2Br$ heterojunctions to effectively remove persistent pollutants from wastewater.

1. Introduction

In recent years, rapid industrialization has significantly exacerbated water pollution and led to an escalating environmental crisis. Industrial wastewater often contains large amounts of synthetic dyes that pose a significant risk to human health and aquatic ecosystems [1,2]. Organic dyes are difficult to degrade naturally because of their stable and intricate chemical structures, rendering them persistent environmental contaminants [3,4]. Among other dyes, Rhodamine B (RhB) is a synthetic xanthene dye that is extensively utilized in the textile industry, biological staining, and glass manufacturing. Its intense fluorescence and bright color make it valuable for industrial purposes; however, its

* Corresponding author. School of Materials Science and Engineering, Nanjing University of Science and Technology, Nanjing, Jiangsu, 210094, China.
** Corresponding author.
*** Corresponding author.
E-mail addresses: Ahsannazir40@yahoo.com (A. Nazir), Ameenaakhan07@yahoo.com (A.T. Rasool), Sundpe301@163.com (D. Sun).

https://doi.org/10.1016/j.mssp.2025.110128
Received 25 July 2025; Received in revised form 24 September 2025; Accepted 7 October 2025

persistent existence in aquatic ecosystems poses a significant threat to the environment [5]. RhB is associated with carcinogenic, mutagenic, and teratogenic effects in humans and animals and has been classified as a Group 3 carcinogen by the International Agency for Research on Cancer (IARC) [6]. In addition to dye contaminants, contaminated water frequently has pathogenic bacteria such as Escherichia coli (E. coli) and Staphylococcus aureus (S. aureus), which can cause serious respiratory, liver, and other health problems, as well as serious health risks such as skin infections, typhoid fever, and diarrhea [7,8]. The Infectious Diseases Society of America (IDSA) estimates that approximately 0.13 billion children under the age of five die each year from diarrheal diseases, with contaminated water containing E. coli being one of the main causes [9]. Despite research into numerous water treatment methods, including membrane filtration, solvent extraction, electrolysis, adsorption, etc. [10–12], many of them encounter difficulties such as high energy consumption, high costs, and insufficient removal of pollutants [6,13]. These shortcomings have led to an increased interest in photocatalytic techniques, which offer advantages such as excellent efficiency, cost-effectiveness, ease of use, minimal toxicity, and environmental compatibility [14,15]. However, photocatalytic materials have significant potential for sustainable wastewater treatment as they enable the simultaneous degradation of organic contaminants and inactivation of bacteria when exposed to visible light.

Recently, bismuth-based photocatalysts have emerged as viable options due to their unique electronic structure and excellent response to visible light. Various bismuth-based materials, including Bi_2S_3, Bi_2O_3, $BiVO_4$, BiOBr, Bi_2WO_6, and $PbBiO_2X$ (X = Br, I, Cl), have been extremely studied owing to their superb photocatalytic properties [16–18]. Among them, $PbBiO_2Br$ stands out as a particularly promising photocatalyst with an ideal band gap of about 2.4–2.6 eV, making it an excellent material for the destruction of organic pollutants [19]. Investigations have demonstrated the improved photocatalytic effectiveness of $PbBiO_2Br$ in eliminating organic contaminants from the environment. For example, Wang and Xiao et al. synthesized porous microspheres and ultrathin nanosheets of $PbBiO_2Br$ using solvothermal approaches, respectively, and exhibited their notable photocatalytic effectiveness for the destruction of organic dyes and antibacterial agents [20,21]. But, the practical photocatalytic applications of pure $PbBiO_2Br$ are significantly constrained by the inadequate production of reactive species and the rapid recombination of photoinduced charge carriers [18]. To overcome these limitations, $PbBiO_2Br$ can be coupled with suitable semiconductors to create heterojunctions, which is a useful method to increase photocatalytic activity. To date, researchers have developed a numerous $PbBiO_2Br$-based heterojunctions to augment the photocatalytic efficiency of pure $PbBiO_2Br$, such as SrTiO3/PbBiO2Br [22], NiO/$PbBiO_2Br$ [23], $PbBiO_2Br$/UiO-66-NH_2 [24], Ag_3PO_4/$PbBiO_2Br$ [25], $PbBiO_2Br$/ZnO [26], and Cu_2O/$PbBiO_2Br$ [27]. However, in order to advance the research of $PbBiO_2Br$ in photodegradation, further $PbBiO_2Br$-based photocatalysts are anticipated to be constructed.

In recent years, silver halide-based photocatalysts, including AgBr, AgCl, and AgI, have garnered significant attention owing to their capacity to enhance photocatalytic efficacy [28,29]. Among them, AgI is considered a promising semiconductor for photocatalytic applications due to its suitable band gap (~2.78 eV), effective absorption of visible light, and high photosensitivity [30,31]. To date, various heterojunction photocatalysts have been developed with AgI to improve photocatalytic efficiency. For instance, Chen et al. developed AgI/$BiVO_4$ composite by the in-situ precipitation technique and showed remarkable photodegradation performance of tetracycline (TC) [32]. Ahmad et al. developed CdS/AgI using the in situ precipitation procedure, which demonstrated exceptional efficacy in degrading TC and methyl orange (MO) [33]. Guan et al. prepared an AgI/$BiVO_4$ composite by a chemical deposition-precipitation method and investigated its photocatalytic activity to inactivate Escherichia coli (E. coli) and eliminate oxytetracycline hydrochloride (OTC-HCl) [31]. Ma et al. constructed an AgI/Ta_2O_{5-x} composite by combining solvothermal and chemical deposition approaches, demonstrating effective photocatalytic capability in the degradation of TC [34]. Given the clear advantages of $PbBiO_2Br$ and AgI semiconductors, the integration of AgI on $PbBiO_2Br$ offers a viable approach to create a novel photocatalyst with an effective heterojunction that can enhance organic contaminants degradation and bacterial inactivation. So far, there are no reports of the development of an AgI@$PbBiO_2Br$ based heterojunction photocatalyst, particularly one synthesized by a simple and economical process. Many current photocatalytic methods for removing organic pollutants are energy-intensive and unfeasible for large-scale use [35,36]. Here, we propose a scalable, facile, and energy-efficient in situ deposition-precipitation approach for the fabrication of AgI@$PbBiO_2Br$. This innovative method addresses a shortcoming in previous research and provides a scalable route for the production of effective catalysts for environmental remediation.

In this work, a novel Z-scheme AgI@$PbBiO_2Br$ photocatalyst was developed in a simple and environmentally friendly process by a facile in situ deposition-precipitation. The photocatalytic ability of the materials under visible light was assessed for the removal of different pollutants. To investigate the multipurpose potential of the AgI@$PbBiO_2Br$ photocatalyst for environmental remediation, its antibacterial activity towards E. coli and S. aureus was also assessed. The synthesized materials were comprehensively characterized using multiple analytical techniques, and their photocatalytic processes were further clarified through electron spin resonance (ESR) analysis and reactive species trapping assays. The stability test for RhB elimination was conducted over four trials using visible light exposure. In addition, density functional theory (DFT) and liquid chromatography-mass spectrometry (LC-MS) were used to investigate the reactive sites of the RhB molecules and their degradation pathways, providing a comprehensive insight into the mechanism of action. This study not only establishes a novel approach for improving the photocatalytic efficacy of AgI@$PbBiO_2Br$ but also broadens its use to multifunctional environmental remediation.

2. Experimentation part

2.1. Materials

Sinopharm Chemical Co., Ltd. supplied potassium iodide (KI), lead nitrate ($Pb(NO_3)_2$), and silver nitrate ($AgNO_3$). Beijing Solarbio Chemical Co., Ltd. provided cetyltrimethylammonium bromide (CTAB). Sigma-Aldrich Co., Ltd. supplied ethylenediaminetetraacetic acid disodium salt (EDTA-2Na), neutral red (NR), RhB, TC, and methyl orange (MO). Energy Chemical Co., Ltd. supplied benzoquinone (BQ). Aladdin Chemical Co., Ltd. supplied bismuth nitrate pentahydrate ($Bi(NO_3)_3{\cdot}5H_2O$) and isopropyl alcohol (IPA). Deionized (DI) water was utilized in the whole experiment.

2.2. Preparation of $PbBiO_2Br$

$PbBiO_2Br$ was produced using a hydrothermal process according to previous literature [35]. In brief, dissolve 1 mmol each of CTAB, $Pb(NO_3)_2$, and $Bi(NO_3)_3{\cdot}5H_2O$ in 40 mL of DI water with constant agitation for 30 min to prepare a homogeneous suspension. The resulting mixture was thereafter agitated for a further half hour after the pH had been adjusted to 14 by adding 2 M NaOH solution. The mixture was placed in a Teflon-lined autoclave and subjected to heating at 180 °C for 12 h. Thereafter, the resulting precipitates were centrifuged, washed, and dried at 50 °C for a whole night. Ultimately, the dried powder was calcined at 400 °C for 2 h to improve its crystallinity, yielding the $PbBiO_2Br$ sample. A schematic illustration of the preparation of $PbBiO_2Br$ photocatalyst is presented in Fig. 1.

2.3. Preparation of AgI@$PbBiO_2Br$

The AgI@$PbBiO_2Br$ composites were prepared by a facile in situ

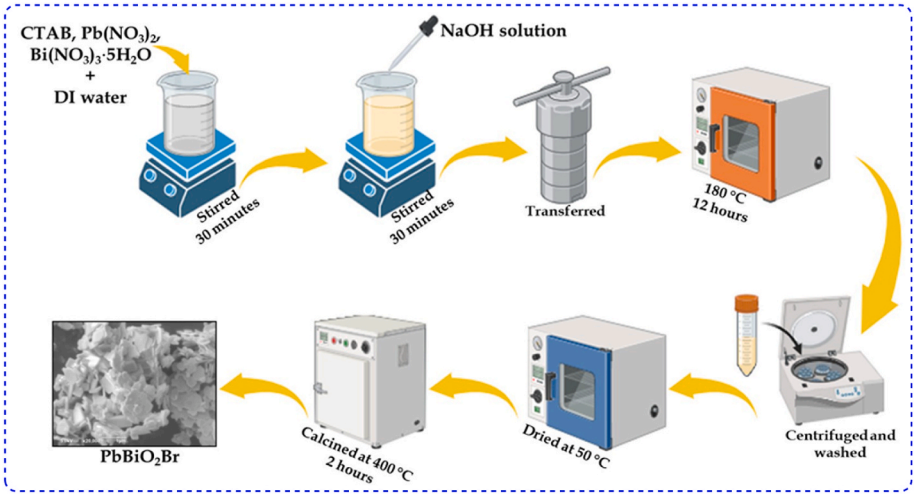

Fig. 1. A schematic diagram of the production process for the $PbBiO_2Br$ photocatalyst.

deposition-precipitation technique. Briefly, 0.5 mmol of $PbBiO_2Br$ powder was added to 25 mL of DI water and subjected to ultrasonic treatment to obtain a homogeneous suspension. Then, $AgNO_3$ (0.281 mmol) was introduced into the above suspension with continuous agitation for 30 min in the dark. Afterward, the KI solution (5 mL) containing 0.281 mmol of KI was gradually incorporated into the earlier suspension. The resulting suspension was agitated for another 2 h to synthesize the sample with the theoretical mass ratio of 20 wt% AgI to $PbBiO_2Br$. The sample was acquired using centrifugation, then washed and dried overnight at 50 °C. The sample was named 20 %-AgI@$PbBiO_2Br$. Similarly, the composites containing 10 wt% and 30 wt% AgI@$PbBiO_2Br$ were also prepared according to the method described above by adjusting the mass ratio of AgI to $PbBiO_2Br$ and the sample was named 10 %-AgI@$PbBiO_2Br$ and 30 %-AgI@$PbBiO_2Br$, respectively. For comparison, pure AgI nanoparticles were prepared under the same conditions without $PbBiO_2Br$. The preparation of the AgI@$PbBiO_2Br$ heterojunction is shown schematically in Fig. 2.

2.4. Characterization

X-ray photoelectron spectroscopy (XPS, PHI QUANTERA II) and X-ray diffraction (XRD, Rigaku/RINT-2000) were used to evaluate the chemical composition and crystalline structure of the prepared samples, respectively. The JEM-F200 microscope was used to obtain high-resolution transmission electron microscopy (HRTEM), energy dispersive spectroscopy (EDS), and TEM images, while a JIB-4700F microscope was used to acquire scanning electron microscopy (SEM). Photoluminescence (PL) spectroscopy (Edinburgh FLS-1000) and UV–vis diffuse reflectance spectroscopy (UV–vis DRS, Shimadzu UV-3600) were utilized to analyze the optical properties. The adsorption/desorption isotherm was utilized to quantify the surface area using a Brunauer-Emmett-Teller (BET, V-Sorb 2800 TP) apparatus. An electrochemical workstation was utilized to assess the charge transfer properties by electrochemical impedance spectroscopy (EIS). A Bruker EMX-A300 spectrometer was used to record ESR spectra and the AB SCIEX Triple TOF 5600+ instrument was used to perform LC-MS. Using the B3LYP/6-31G+(d, p) basis set in the Gaussian09 program, the shape and vibrational frequencies of the RhB molecules were optimized for the DFT calculations [37]. Natural bond orbital (NBO) analysis was employed to examine the natural population distributions of cation, anion, and RhB radical species.

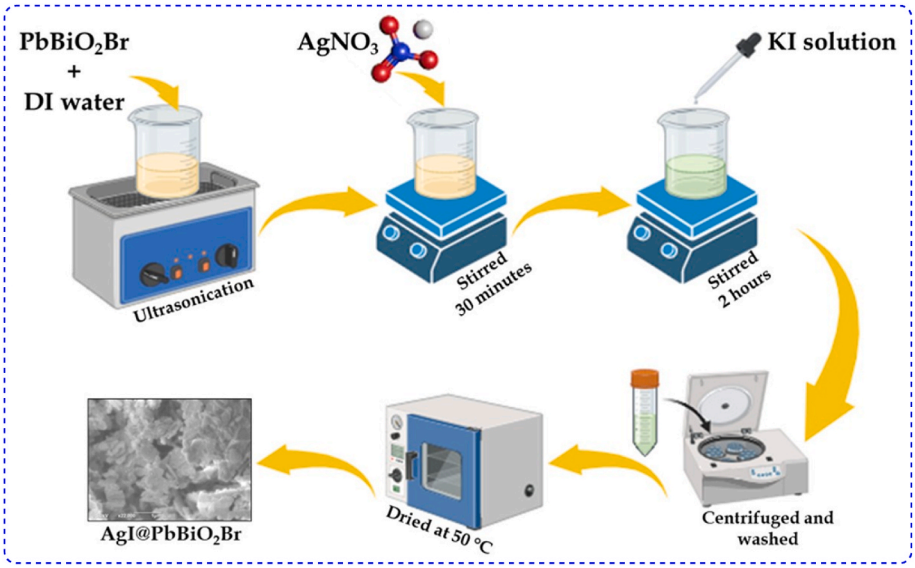

Fig. 2. A schematic diagram of the production process for the AgI@$PbBiO_2Br$ heterojunction.

2.5. Photocatalytic degradation evaluation

The breakdown of RhB was employed to assess the photocatalytic efficiency of the produced materials when exposed to visible light using a 500 W LED floodlight (50 Hz, AC 220 V) as an illumination source. The floodlight with the white LED was placed in the middle over the beaker containing the reaction mixture. In each experiment, 50 mL of an aqueous RhB solution containing 10 mg/L was used to add 50 mg of the photocatalyst. In order to establish an equilibrium between the RhB molecules and the surface of the photocatalyst, the solution was agitated in the dark for half an hour before exposure to light. Once equilibrium was achieved, the photodegradation process was initiated by turning on the visible light source. 2 mL aliquots of the suspension were extracted at regular times (usually every 10 min) and filtered right away via a membrane with a 0.22 μm to get rid of the photocatalyst particles. The concentration of RhB in the clear filtrate was ascertained by measuring the absorption wavelength characteristic for RhB (λ = 554 nm) using a UV–vis spectrophotometer. The following formula can be used to determine the photodegradation ratio of a pollutant [35].

$$\text{Photodegradation}\ (\%) = (C_0 - C) / C_0 \times 100\% \quad (1)$$

Here, pollutant concentrations in the photocatalytic process at initial and final are denoted by C_0 and C, respectively.

2.6. Antibacterial activity evaluation

The antibacterial effectiveness of the 20 %-AgI@$PbBiO_2Br$ was specifically assessed towards E. coli and S. aureus. The initial procedures for the antibacterial assay involved sterilizing all culture plates, media, and equipment via autoclaving at high temperature and pressure to guarantee aseptic conditions. In the antibacterial studies, the bacterial cultures were initially cultivated to the logarithmic phase and then diluted with sterile water to achieve a specific concentration in colony-forming units per milliliter (CFU/mL). To create the photocatalyst suspension, 1 mg of the photocatalyst was measured, dispersed in 1 mL of sterile distilled water, and sonicated to acquire a uniform suspension. In the experiment, 200 μL of the diluted bacterial suspension was combined with 200 μL of the 1 mg/mL photocatalyst suspension. The mixture was then irradiated with visible LED light to initiate the photocatalytic antibacterial reaction. After irradiation, each treated suspension was spread evenly on sterile solid LB agar plates. The plates were incubated at 37 °C for 24 h. To evaluate the 20 %-AgI@$PbBiO_2Br$ antibacterial efficacy, the number of bacterial colonies on each plate was meticulously counted after incubation. The results were recorded visually by photographing the cultured plates to obtain a clear comparison of bacterial growth suppression. Control studies were conducted under the same conditions without treatment with the photocatalyst.

3. Results and discussion

3.1. Materials characterization

XRD was employed to examine the crystal structures of the produced samples, as illustrated in Fig. 3. In pure $PbBiO_2Br$, all diffraction peaks correspond to the tetragonal structure of $PbBiO_2Br$ as per JCPDS No. 38–1008 [38], and there is no additional contaminated phase detected, indicating that the produced $PbBiO_2Br$ is highly pure. The AgI shows diffraction peaks at 2θ values of 22.3°, 23.7°, 25.4°, 39.3°, 42.7°, and 46.23° associated with crystal planes (100), (002), (101), (110), (103), and (112) of AgI as per JCPDS No. 09–0374 [39,40]. The XRD patterns of AgI@$PbBiO_2Br$ composites show a clear coexistence of two different phases, AgI and $PbBiO_2Br$, confirming the successful incorporation of AgI into $PbBiO_2Br$. The intensity of the diffraction peaks associated with AgI increased with increasing weight ratio of AgI, consistent with the higher amounts of AgI incorporated during the fabrication process. So,

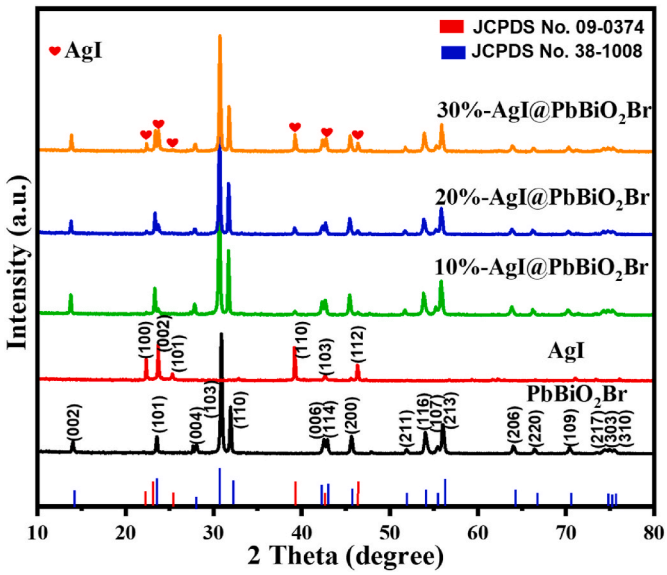

Fig. 3. XRD patterns of $PbBiO_2Br$, AgI, and AgI@$PbBiO_2Br$ with different weight ratios.

the increasing AgI content in the composite can be recognized by the increasing intensity of the peaks. Notably, all composites exhibited identical diffraction peaks for both AgI and $PbBiO_2Br$, suggesting that the incorporation of AgI did not substantially modify the phase or crystal structure of $PbBiO_2Br$. Thus, the XRD study confirms the successful preparation of AgI@$PbBiO_2Br$ composites.

The chemical composition of $PbBiO_2Br$, AgI, and 20 %-AgI@$PbBiO_2Br$ was investigated using XPS. According to the XPS survey spectra (Fig. 4a) for $PbBiO_2Br$, AgI, and 20 %-AgI@$PbBiO_2Br$, the elements Pb, Br, Bi, and O can be observed in $PbBiO_2Br$, the elements Ag and I are found in AgI and the elements Pb, Br, Bi, O, Ag and I are present in 20 %-AgI@$PbBiO_2Br$. In Fig. 4b, the Pb 4f peaks in $PbBiO_2Br$ at 137.95 and 142.84 eV are allocated to Pb $4f_{7/2}$ and Pb $4f_{5/2}$ of Pb^{2+}, respectively [24]. Fig. 4c shows the Bi 4f peaks in $PbBiO_2Br$ at 158.88 and 164.27 eV, which correspond to Bi $4f_{7/2}$ and Bi $4f_{5/2}$ of Bi^{3+}, respectively [41]. The O 1s peaks in $PbBiO_2Br$ (Fig. 4d) appear at 529.99 and 531.24 eV, which can be associated with the lattice oxygen in $PbBiO_2Br$ [42]. The Br 3d peaks in $PbBiO_2Br$ (Fig. 4e) are observed at 68.20 eV for Br $3d_{5/2}$ and 69.19 eV for Br $3d_{3/2}$, which are associated with Br^- [43]. The Ag 3d peaks in AgI at 367.88 eV for Ag $3d_{5/2}$ and 373.89 eV for Ag $3d_{3/2}$ (Fig. 4f) [44]. The I 3d peaks in AgI (Fig. 4g) at 619.21 and 630.69 eV are ascribed to I $3d_{5/2}$ and I $3d_{3/2}$ of I^-, respectively [45,46]. Interestingly, the XPS spectra of the 20 %-AgI@$PbBiO_2Br$ show that the binding energies of Pb 4f, Bi 4f, O 1s, and Br 3d shift to slightly lower binding energies compared to pure $PbBiO_2Br$, while the binding energies of Ag 3d and I 3d in 20 %-AgI@$PbBiO_2Br$ shift to slightly higher values in 20 %-AgI@$PbBiO_2Br$ compared to pure AgI. The observed changes in binding energy are caused by the altered electron density at the $PbBiO_2Br$ and AgI surfaces in the 20 %-AgI@$PbBiO_2Br$ heterostructure, indicating the presence of strong interfacial interactions between them and the successful formation of a heterojunction [38]. Similar phenomena were observed in previous studies [47,48], so the XPS study also validated the successful fabrication of the 20 %-AgI@$PbBiO_2Br$.

The morphology of the prepared $PbBiO_2Br$ and the 20 %-AgI@$PbBiO_2Br$ composite was examined using SEM, as depicted in Fig. 5. Fig. 5a illustrates that $PbBiO_2Br$ displays a uniform, sheet-like morphology. Fig. 5b shows that in the 20 %-AgI@$PbBiO_2Br$ composite, the AgI nanoparticles are evenly distributed and tightly anchored on the $PbBiO_2Br$ surface. TEM image of the 20 %-AgI@$PbBiO_2Br$ (Fig. 5c) further verifies the robust adhesion of AgI nanoparticles to the $PbBiO_2Br$ surface, matching the results obtained from SEM analysis. Two separate

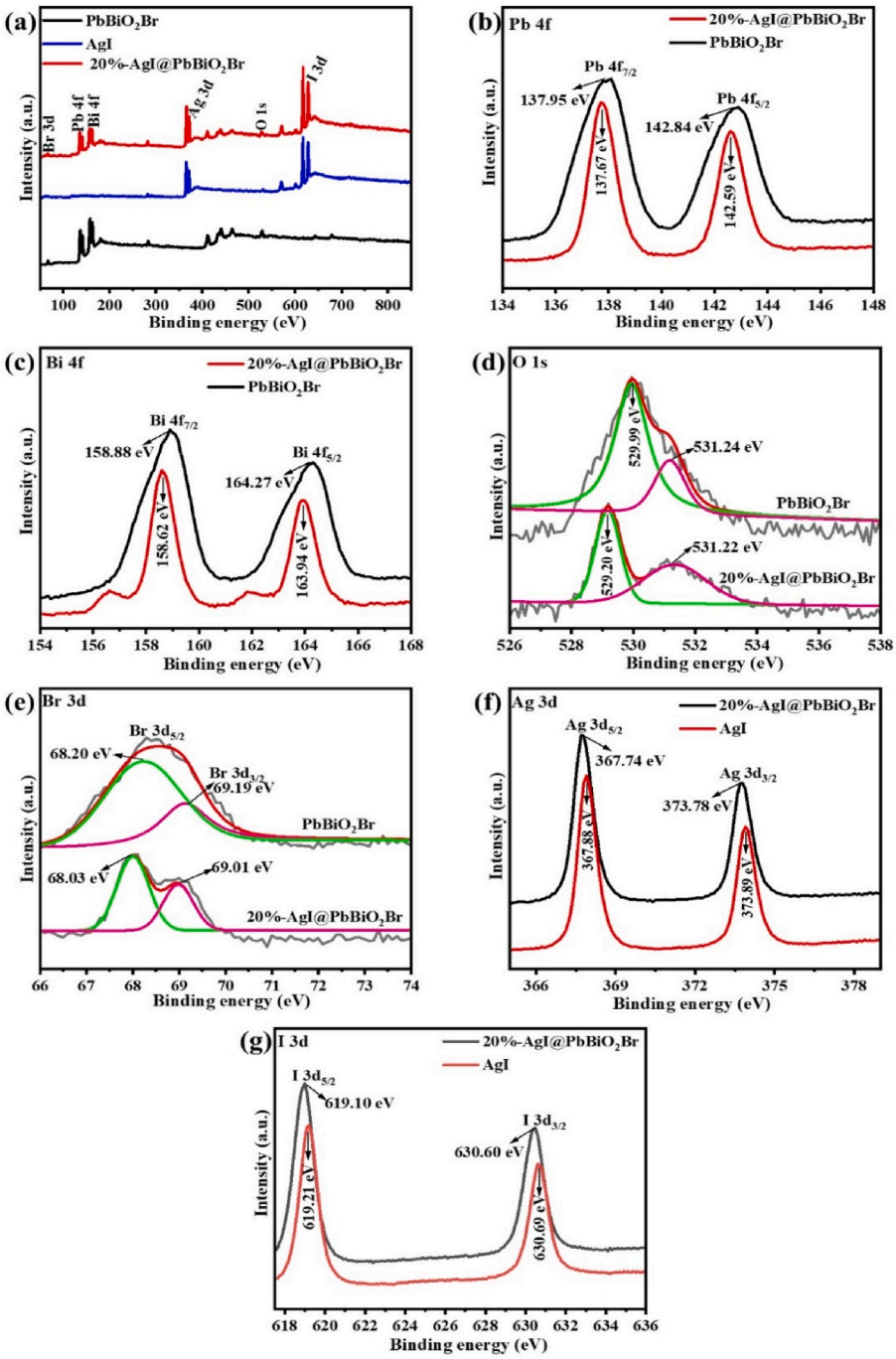

Fig. 4. XPS spectra of $PbBiO_2Br$, AgI, and 20 %-AgI@$PbBiO_2Br$ (a) the surveys, (b) Pb 4f, (c) Bi 4f, (d) O 1s, (e) Br 3d, (f), Ag 3d, and (g) I 3d.

lattice fringes can be seen in the HRTEM image (Fig. 5d), with a distance of 0.235 nm for the AgI (1 1 0) plane and 0.290 nm for the $PbBiO_2Br$ (1 0 3) plane [33,49]. Fig. S1a–f demonstrate the EDS images, confirming the existence of O, Br, Ag, I, Pb, and Bi in the 20 %-AgI@$PbBiO_2Br$ heterojunction. The elemental distributions are consistent with the XPS results. Furthermore, Fig. S2 displays the EDS spectrum in conjunction with the corresponding elemental content (atomic%). These results demonstrate that the 20 %-AgI@$PbBiO_2Br$ heterojunction was successfully prepared, in which AgI and $PbBiO_2Br$ exhibit a strong interfacial interaction. This strong bond is expected to improve the charge separation and transport in the AgI@$PbBiO_2Br$ heterojunction.

UV–vis DRS was used to evaluate the light absorption properties of the prepared samples, as shown in Fig. 6a. Pure $PbBiO_2Br$ and AgI show absorption edges at about 510 nm and 446 nm, respectively. The AgI@$PbBiO_2Br$ composites exhibited significantly broader light absorption in the 200–800 nm range compared to the individual photocatalysts. The synergistic co-catalytic interaction between AgI and $PbBiO_2Br$ is mainly responsible for the improvement of optical absorption in the visible region of AgI@$PbBiO_2Br$ composites. The Tauc equation was used to calculate the band gap energy (E_g) of the samples: $\alpha h\nu = A\ (h\nu\text{-}E_g)^{n/2}$. In this context, h implies to the Planck constant, α represents the absorption coefficient, A denotes a proportionality constant, ν signifies the light frequency, and n represents the types of optical transitions that occur in the semiconductor; a direct transition is represented by n = 1, and an indirect transition is represented by n = 4. According to previous studies, both AgI and $PbBiO_2Br$ have a direct band

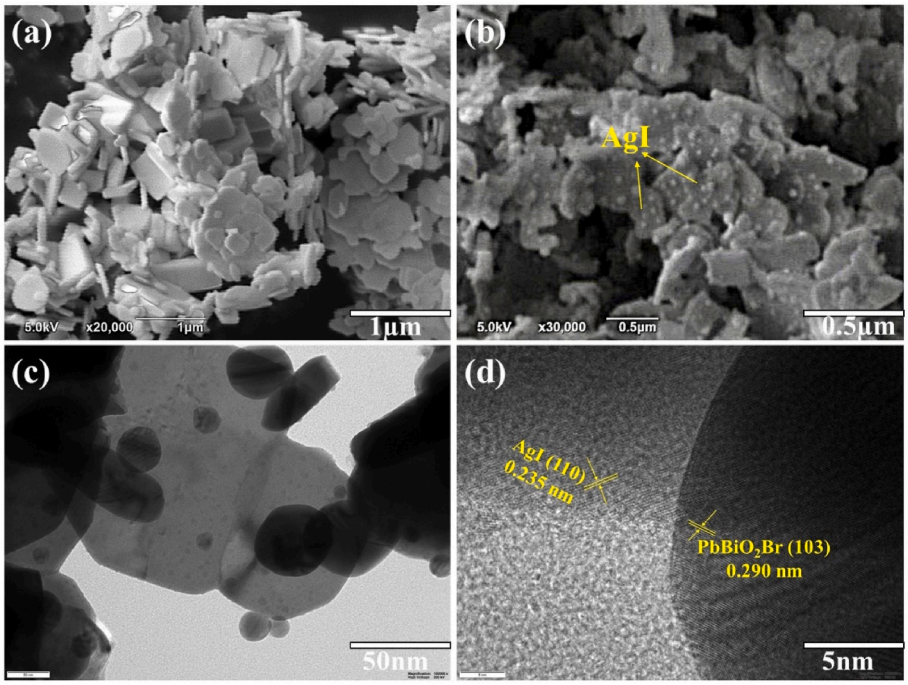

Fig. 5. SEM of (a) $PbBiO_2Br$, (b) 20 %-AgI@$PbBiO_2Br$, (c) TEM of 20 %-AgI@$PbBiO_2Br$, and (d) HRTEM of 20 %-AgI@$PbBiO_2Br$.

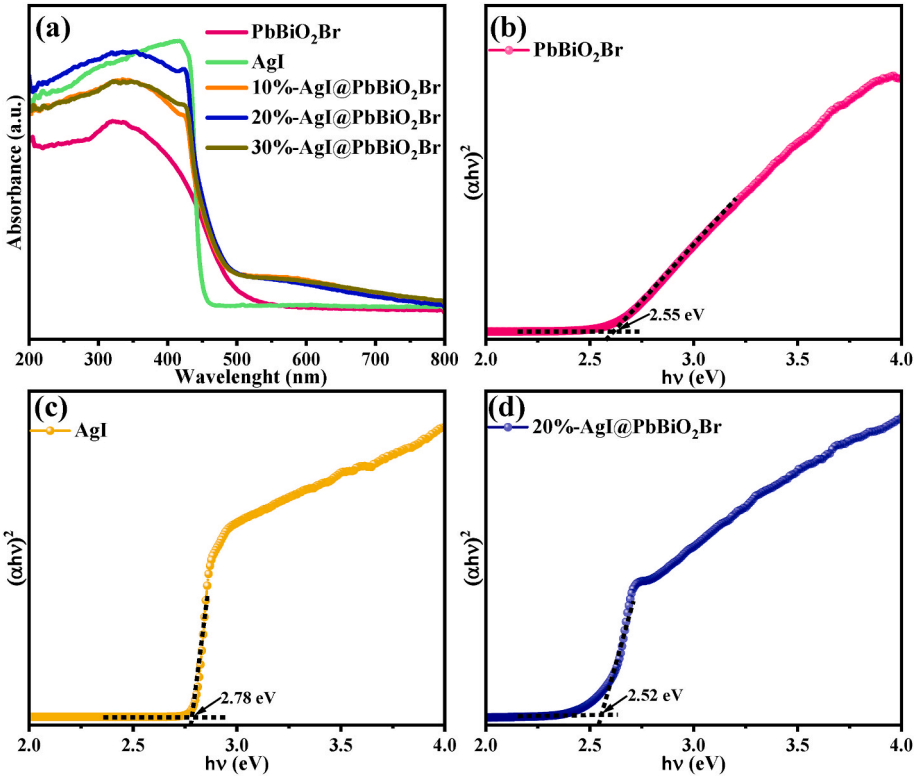

Fig. 6. (a) UV–vis DRS for all samples and (b–d) the bandgap spectra of $PbBiO_2Br$, AgI, and 20 %-AgI@$PbBiO_2Br$.

gap (n = 1). [19,50]. Thus, the E_g of AgI and $PbBiO_2Br$ were determined based on the premise of direct band gaps. As shown in Fig. 6b–d, the estimated E_g for $PbBiO_2Br$, AgI, and the 20 %-AgI@$PbBiO_2Br$ are 2.55, 2.78, and 2.52 eV, respectively. The conduction band (E_{CB}) of $PbBiO_2Br$ and AgI was determined by a combination of XPS valence band (E_{VB}) spectra and optical band gap values from UV–vis DRS analysis. Fig. S3a, b shows that the E_{VB} of $PbBiO_2Br$ and AgI is 1.67 and 0.32 eV, respectively, which aligns with the prior findings [35,51]. Thus, the obtained E_{CB} of $PbBiO_2Br$ and AgI is −0.88 and −2.46 eV, respectively, derived from the formula $E_g = E_{VB} - E_{CB}$ [52]. These band positions are crucial for elucidating the charge transfer behavior and the underlying photocatalytic mechanisms within the heterostructure, as they determine the

migration routes of the photogenerated charge carriers and are essential for facilitating effective electron-hole separation upon light irradiation.

In order to determine the surface area of the $PbBiO_2Br$ and 20 %-AgI@$PbBiO_2Br$, the BET nitrogen adsorption/desorption isotherms were employed (Fig. S4). In the case of $PbBiO_2Br$, the particular surface area was estimated to be approximately 2.89 m^2/g (pore volume 0.005 cm^3/g), while for 20 %-AgI@$PbBiO_2Br$ it is approximately 1.55 m^2/g (pore volume 0.003 cm^3/g). The reduction of the surface area of 20 %-AgI@$PbBiO_2Br$ is probably due to the deposition of AgI nanoparticles in the interlayers or on the surface of the $PbBiO_2Br$ sheet, as shown by the diminished pore volume of $PbBiO_2Br$ after AgI intercalation. This BET result is consistent with results reported in previous research for other AgI-based composites [53,54].

3.2. Evaluation of photocatalytic degradation

The photocatalytic properties of the materials were evaluated by testing the elimination of RhB under visible light irradiation. Fig. 7a, b show that pure RhB is only minimally degraded under visible light, emphasizing that a catalyst is required to enable effective photodegradation. Pure $PbBiO_2Br$ exhibits relatively insufficient photocatalytic activity, achieving only 46.77 % RhB degradation after 70 min of irradiation. In contrast, pure AgI showed a significantly better performance and degraded about 73.58 % of RhB under identical conditions. Compared to the individual components, the AgI@$PbBiO_2Br$ composites displayed substantially enhanced photocatalytic activity. The degradation efficiency improved with increasing AgI content in the composite and reached a maximum when the AgI loading was 20 %. The 20 %-AgI@$PbBiO_2Br$ composite achieved an impressive RhB degradation of 98.72 % within 70 min of visible light exposure. The improved performance of AgI-modified $PbBiO_2Br$ is primarily because AgI and $PbBiO_2Br$ form an efficient heterojunction that facilitates the effective segregation of photoinduced electron-hole pairs, lowers their recombination, and boosts photocatalytic effectiveness. Conversely, the photocatalytic activity of the AgI@$PbBiO_2Br$ (like 30 %-AgI@$PbBiO_2Br$) composite decreased when the AgI content exceeded 20 %. This

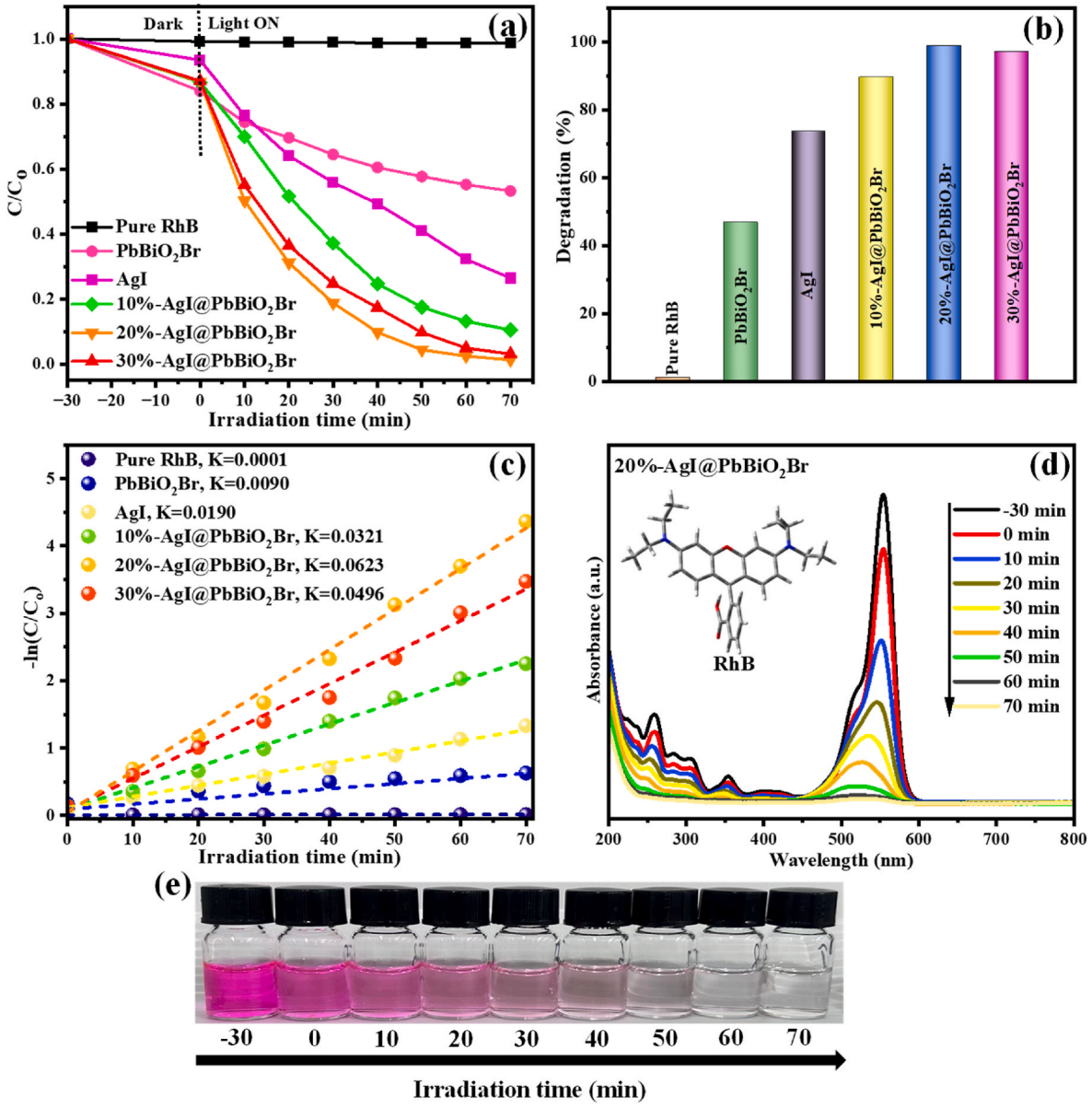

Fig. 7. (a) Photodegradation curves, (b) photodegradation efficiency, (c) pseudo-first-order kinetics of RhB removal for all samples, (d) UV–vis spectra of RhB removal by 20 %-AgI@$PbBiO_2Br$, and (e) color variation of RhB solutions with time by 20 %-AgI@$PbBiO_2Br$. (For interpretation of the references to color in this figure legend, the reader is referred to the Web version of this article.)

decrease in performance is likely due to the excessive AgI nanoparticles obstructing the $PbBiO_2Br$ surface from light irradiation and thereby reducing the generation of photoinduced charge carriers, which are vital for the degradation process [32,55]. Consequently, the control of AgI content is crucial to achieve the best performance of AgI@$PbBiO_2Br$--based photocatalysts. In addition, the experimental data were evaluated via a pseudo-first-order kinetic model to obtain a better understanding of the photocatalytic oxidation process, which is represented by the following equation: $\ln C/C_0 = Kt$, where K designates the reaction rate constant, t indicates the irradiation time, C_0 and C refer to the initial and ultimate concentrations of the RhB solution [56]. The kinetic analysis displays a clear pattern in the photocatalytic efficacy of the investigated materials (Fig. 7c). The K values obtained for the materials are shown in the following order: 20 %-AgI@$PbBiO_2Br$ > 30 %-AgI@$PbBiO_2Br$ > 10 %-AgI@$PbBiO_2Br$ > AgI > $PbBiO_2Br$. Among them, the 20 %-AgI@$PbBiO_2Br$ composite exhibited the maximum K value of 0.0623 min^{-1}, demonstrating excellent photocatalytic effectiveness. The findings demonstrated that the integration of AgI to the $PbBiO_2Br$ matrix both improved the light absorption in the visible spectrum and increased the overall degradation activity through a synergistic effect. Importantly, the photocatalytic activity was significantly affected by the AgI loading ratio. It was found that an optimum AgI content of 20 % resulted in maximum degradation efficiency and kinetic rate. Fig. 7d shows the changes in the UV–vis absorption spectra during the photodegradation of RhB using the 20 %-AgI@$PbBiO_2Br$. With increasing duration of visible light irradiation, the distinctive RhB absorption peak at 554 nm exhibits a pronounced blue shift to 520 nm, together with a significant decrease in peak intensity. This shift suggests sequential N-deethylation of RhB during the decomposition process, which is consistent with results reported by other researchers [5,57]. At the same time, the pink color of the aqueous RhB solution decreases over time when treated with 20 %-AgI@$PbBiO_2Br$ and eventually disappears completely, as shown in Fig. 7e.

The photocatalytic efficacy of the 20 %-AgI@$PbBiO_2Br$ heterojunction was also assessed by studying the decomposition of additional organic dyes such as MO and NR when exposed to visible light. Fig. 8a displays the UV–vis absorption spectra of MO during its photodegradation by 20 %-AgI@$PbBiO_2Br$. As irradiation time increases, the distinctive absorption peak of MO at 464 nm consistently diminishes, signifying the gradual degradation of the dye molecules. The peak almost disappeared after 30 min of exposure to visible light, indicating that MO was almost completely degraded. The MO dye was successfully removed, as shown by the complete disappearance of the orange color with time in the MO solution (Fig. 8c). Similarly, the photodegradation behavior of NR by 20 %-AgI@$PbBiO_2Br$ is shown in Fig. 8b. With increasing irradiation time, the absorption peak of NR at 525 nm gradually decreases until it almost completely disappears after 60 min, indicating extensive degradation of NR. Fig. 8d shows that the red color of the NR solution completely disappears with time after 60 min, demonstrating the effective degradation of NR by 20 %-AgI@$PbBiO_2Br$. These results confirm that the AgI@$PbBiO_2Br$ photocatalyst exhibits broad photocatalytic efficiency and effectively degrades a range of dyes beyond RhB, including both anionic dye (MO) and cationic dye (NR).

Although dye assays under visible light irradiation can be affected by dye sensitization, in which excited dye molecules transfer electrons to the catalyst [58,59]. We further evaluated the photodegradation of TC antibiotic, a pollutant with a lower susceptibility to sensitization (Fig. S5). No substantial removal was observed with pure TC. Conversely, pure $PbBiO_2Br$ and AgI achieved a removal of 47.6 % and 69.4 %, respectively, within 60 min. As anticipated, 20 %-AgI@$PbBiO_2Br$ demonstrated the highest efficiency of 96.7 %, confirming its superior efficacy in degrading dyes and TC antibiotic. The substantial removal of TC validates the intrinsic visible light activity of the catalyst. The increased degradation activity is due to the creation of a heterojunction between AgI and $PbBiO_2Br$, which increases effective charge separation and visible light absorption, thus enabling the decomposition of organic pollutants. As listed in Table S1, the AgI@$PbBiO_2Br$ composite exhibited superior photodegradation performance compared to numerous recently reported photocatalysts. This exceptional performance underscores the remarkable potential of AgI@$PbBiO_2Br$ for practical applications in wastewater treatment, especially in the effective elimination of dye impurities under visible light irradiation.

3.3. Stability investigation

The stability of the 20 %-AgI@$PbBiO_2Br$ composite was evaluated via four successive cycles of photocatalytic breakdown of RhB when exposed to visible light. After four cycles, the photodegradation rate of RhB decreases only slightly (Fig. 9a and b), signifying that the 20 %-AgI@$PbBiO_2Br$ retains its exceptional stability. XRD study of the 20 %-AgI@$PbBiO_2Br$ before and following the deterioration cycles (Fig. 9c) indicates that the crystal structure of the composite stays largely unaltered, with no notable alterations in diffraction peaks. XPS spectra of the before and after (Fig. S6a–g) indicate that the elemental composition and chemical states of the 20 %-AgI@$PbBiO_2Br$ composite remain stable, exhibiting no significant changes after four cycles. The results

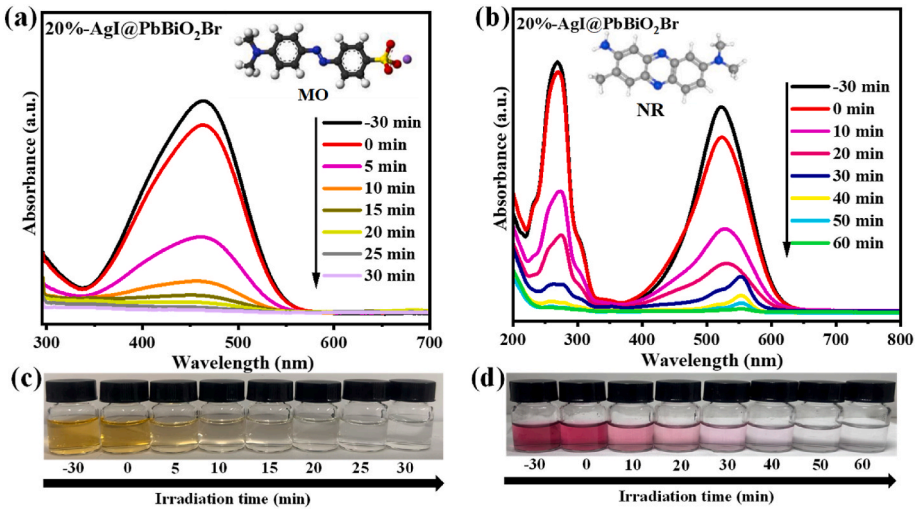

Fig. 8. (a, b) UV–vis spectra of MO and NR removal by 20 %-AgI@$PbBiO_2Br$ and (c, d) color variation of MO and NR solutions with time by 20 %-AgI@$PbBiO_2Br$. (For interpretation of the references to color in this figure legend, the reader is referred to the Web version of this article.)

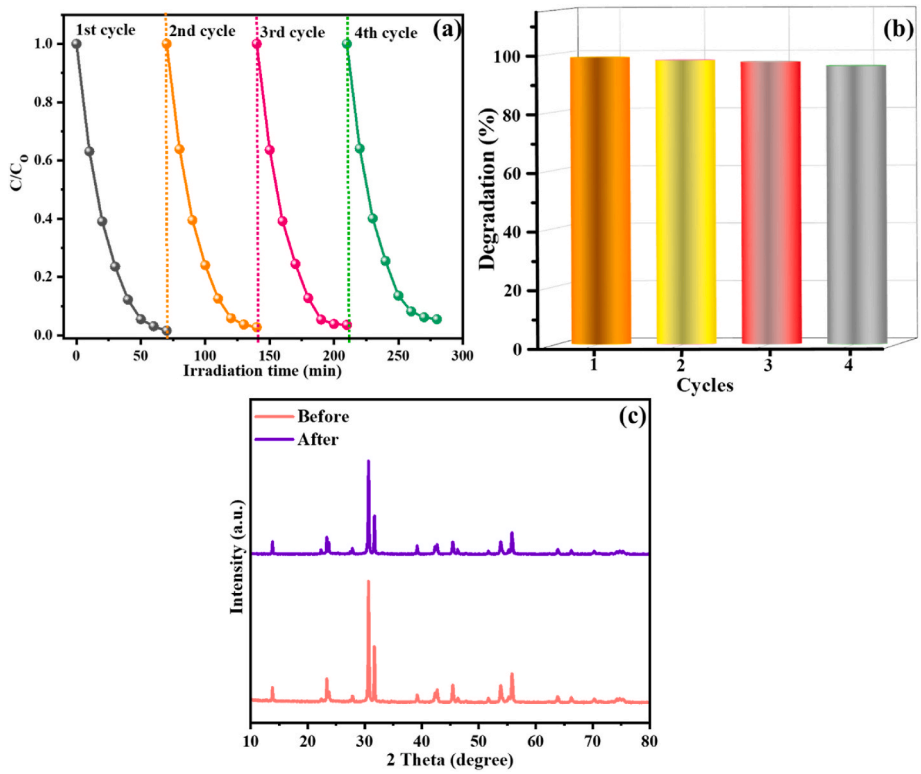

Fig. 9. The cycle runs for RhB removal efficacy by 20 %-AgI@PbBiO$_2$Br (a) photodegradation curves, (b) photodegradation efficiency, and (c) XRD spectra of before and after 20 %-AgI@PbBiO$_2$Br.

collectively indicate that the 20 %-AgI@PbBiO$_2$Br composite displays dependable long-term photocatalytic activity and constant efficacy in the destruction of RhB, affirming its superior stability.

3.4. DFT analysis and possible removal routes of RhB

In order to identify potential reactive sites and intermediates of RhB decomposition, the decomposition processes were investigated using DFT simulations and LC-MS. Fig. 10a–c shows the structural optimization of the RhB molecule, the highest occupied molecular orbital (HOMO), the lowest unoccupied molecular orbital (LUMO) and the molecular electrostatic potential (MEP) mapping. The region of the molecule capable of donating an electron is referred to as the HOMO, while the region that cans accept an electron is termed the LUMO [60]. The electronic structure shows HOMO is at −5.290 eV, while the LUMO is at −2.136 eV, resulting in a moderate energy gap (ΔE) of 3.154 eV. The MEP mapping color scale ranges from -7.145×10^{-2} to 7.145×10^{-2} Hartree, with different colors indicating various electrostatic potential values on the surface, such as red regions indicating high electron density (nucleophilic sites) and blue regions signifying low electron

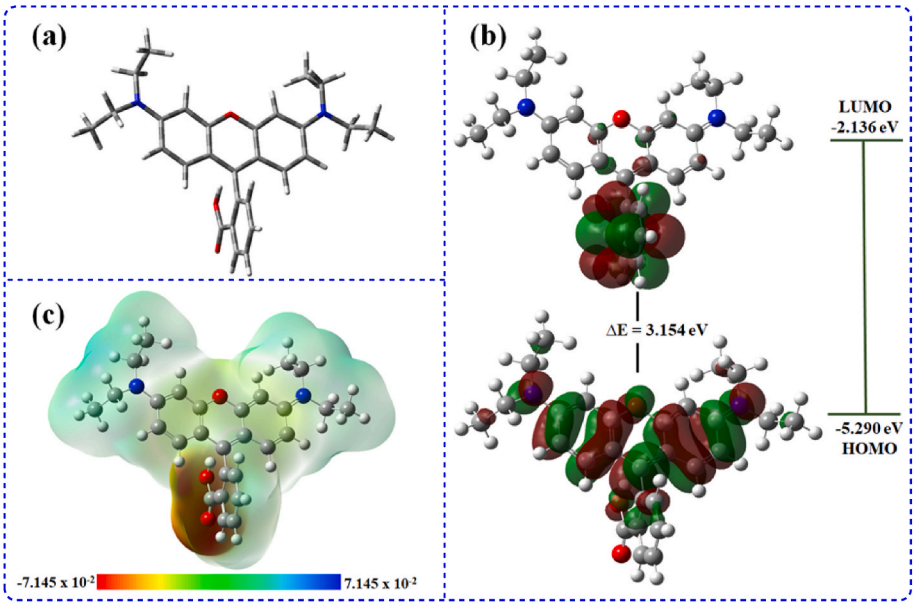

Fig. 10. (a) DFT optimized structure, (b) LUMO-HOMO, and (c) MEP mapping of RhB.

density (electrophilic sites) [61]. To assess the overall chemical reactivity of the RhB molecule, it is important to examine the Fukui indices. The Fukui function derived from Natural Population Analysis (NPA), is an important tool to evaluate the chemical reactivity by analyzing the charge distributions in the RhB cationic (f^+), RhB radical (f^0), and RhB anionic (f^-) states. A maximum f^0 value for certain atomic sites means an increased probability of attack by free radicals [62]. Table S2 shows that the important reactive sites in the RhB molecular structure are represented by the f^0 values, indicating that reactive species are likely to attack mainly C-19 (0.6334), N-15 (0.1291), and O-33 (0.5278).

LC-MS analysis was utilized to identify and verify the intermediates generated during the photodegradation of RhB by 20 %-AgI@$PbBiO_2Br$. Fig. 11 and Table S3 show the potential removal routes of RhB, which are consistent with the results of previous studies [63–65]. In route I, the RhB molecule ($m/z = 443$) is attacked by reactive radicals generated during the photocatalytic process, leading to deethylation and the creation of *P1* ($m/z = 415$), which is then further deethylated to produce *P2* ($m/z = 359$). After deamination and decarboxylation of *P2*, *P3* ($m/z = 285$) is formed. In route II, reactive radicals attacked RhB and generated the intermediate *P1* ($m/z = 415$), which is later further deethylated to generate *P4* ($m/z = 331$). Furthermore, the intermediates *P5-P9* with *m/z* values of *177*, *156*, *118*, *86,* and *46* indicate the fragmentation of the aromatic ring, which leads to the decomposition of the chromophore structure into smaller molecules. Ultimately, these smaller molecules are broken down by the photocatalytic process into inorganic products and harmless small molecules.

3.5. Antibacterial studies

Wastewater often contains harmful bacteria that pose a significant risk to public health. A photocatalytic antibacterial investigation was carried out to test the practical applicability of 20 %-AgI@$PbBiO_2Br$ using E. coli and S. aureus as model bacteria. As depicted in Fig. 12a and b, the control tests carried out both in the dark and in visible light showed no significant antibacterial effect. However, the bactericidal efficacy of 20 %-AgI@$PbBiO_2Br$ was initially tested in the dark. No significant inhibitory effect against E. coli and S. aureus was observed in the dark, indicating the favorable biocompatibility of 20 %-AgI@$PbBiO_2Br$ in the dark. The photocatalytic antibacterial activity of 20 %-AgI@$PbBiO_2Br$ was significantly increased by irradiation with visible light using a 500 W LED light source. The survival rate of E. coli and S. aureus decreased to around 0.01 % after 20 min of illumination, and the bactericidal efficiency reached 99.99 % (Fig. 12c and d), indicating almost complete inactivation of the bacterial population. These results show that 20 %-AgI@$PbBiO_2Br$ exhibits excellent photocatalytic antibacterial activity under visible light, highlighting its enormous potential for real-world use in cleaning up polluted wastewater.

3.6. Possible photodegradation mechanism

The fundamental mechanism of contaminant destruction in a typical photocatalytic system entails the production and involvement of reactive species, namely •OH, h^+, and $•O_2^-$. To recognize the primary reactive species involved in the photodegradation of RhB, a series of radical trapping studies were performed utilizing the 20 %-AgI@$PbBiO_2Br$ heterojunction photocatalyst. Particular scavengers were utilized to specifically neutralize distinct reactive species: BQ for $•O_2^-$, EDTA-2Na for h^+, and IPA for •OH. The findings of these tests (Fig. 13a and b) indicated that the incorporation of EDTA-2Na and BQ markedly inhibited the photocatalytic decomposition efficacy of RhB, underscoring the essential roles of h^+ and $•O_2^-$ in the degradation mechanism. The addition of IPA led to a negligible decrease in degrading performance, indicating that •OH radicals contribute minimally and supportively to the overall process. The observed trend was corroborated by the computed first-order rate K, which was determined to be 0.0072 min^{-1}, 0.0103 min-1, and 0.0315 min^{-1} for systems with EDTA-2Na, BQ, and

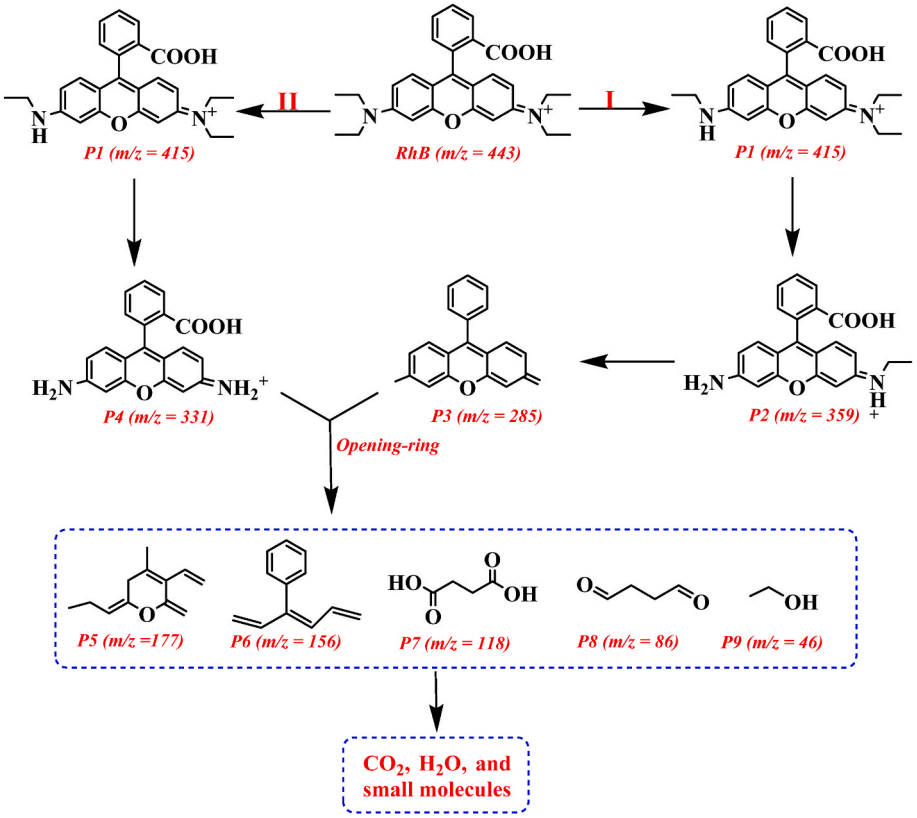

Fig. 11. A possible photodegradation pathway of RhB with 20 %-AgI@$PbBiO_2Br$ heterojunction.

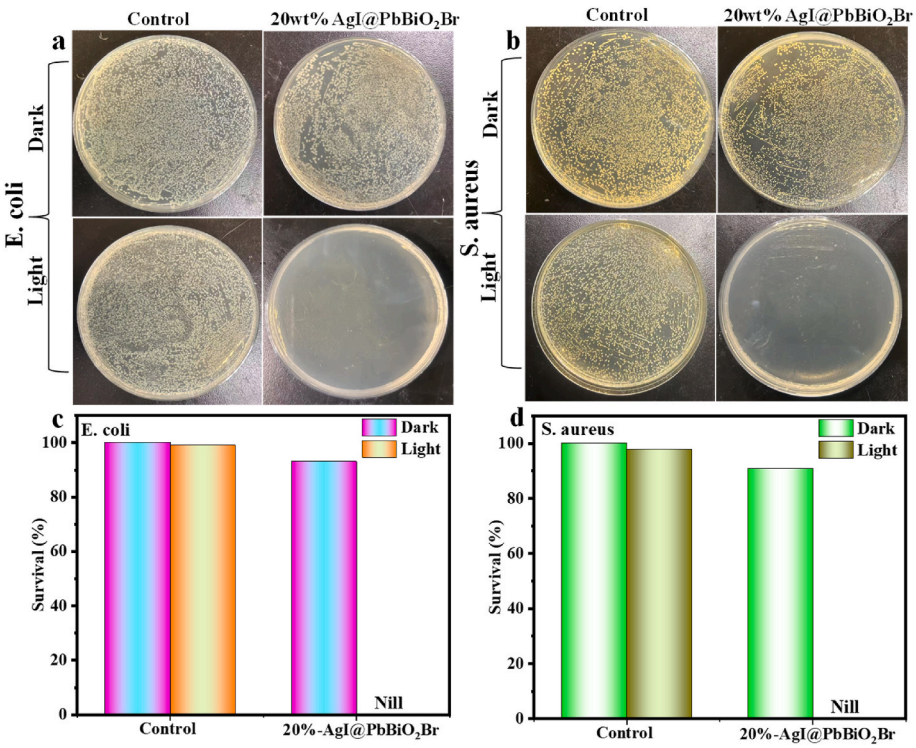

Fig. 12. Antibacterial test of 20 %-AgI@$PbBiO_2Br$ on (a) E. coli, (b) S. aureus, (c, d) survival rate of E. coli and S. aureus.

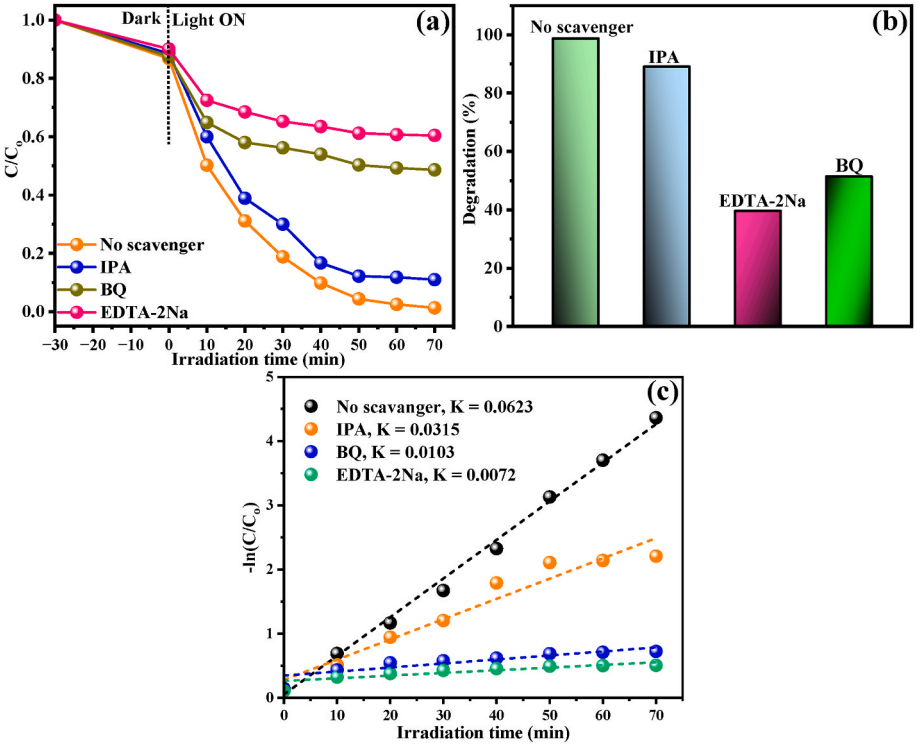

Fig. 13. (a) Photodegradation curves of RhB by 20 %-AgI@$PbBiO_2Br$ with several scavengers under visible light exposure, (b) photodegradation efficiency, and (c) pseudo-first-order kinetics.

IPA, respectively (Fig. 13c). The findings collectively demonstrate that photogenerated h^+ and $\bullet O_2^-$ are the key active species facilitating the photodegradation of RhB, whereas •OH plays a minor role.

The ESR analysis also confirmed the creation of $\bullet O_2^-$ and •OH radicals in the 20 %-AgI@$PbBiO_2Br$. Fig. 14a, b demonstrates that DMPO-$\bullet O_2^-$ and DMPO-•OH exhibit distinct signals upon 10 min of visible light irradiation, whereas no discernible signals are present in darkness, confirming that $PbBiO_2Br$ and 20 %-AgI@$PbBiO_2Br$ may produce $\bullet O_2^-$ and •OH radicals through visible light exposure. Furthermore, the pronounced peak intensities of DMPO-$\bullet O_2^-$ and DMPO-•OH in 20

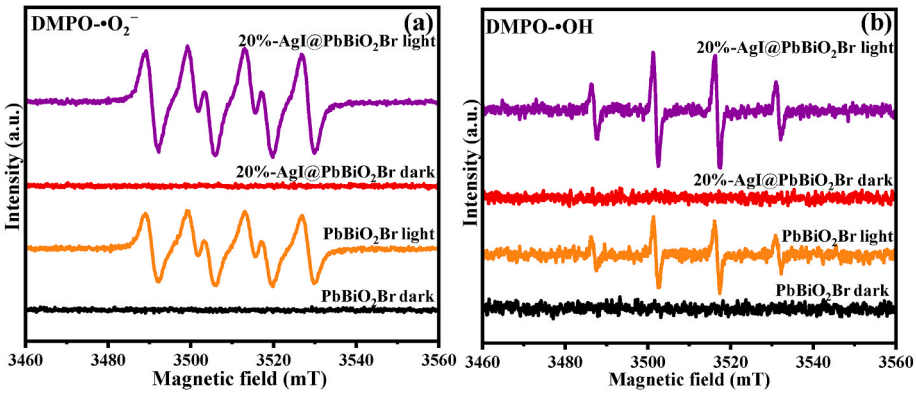

Fig. 14. ESR spectra of pure $PbBiO_2Br$ and 20 %-AgI@$PbBiO_2Br$ in the dark and under visible light exposure, (a) DMPO-•O_2^- and (b) DMPO-•OH.

%-AgI@$PbBiO_2Br$ significantly exceed those observed in pure $PbBiO_2Br$, reinforcing the hypothesis that 20 %-AgI@$PbBiO_2Br$ may augment the creation of •O_2^- and •OH radicals under visible light, hence enhancing photocatalytic efficiency. The trapping studies and ESR investigation validated the key involvement of reactive species (h^+, •O_2^-, •OH) in the degradation of RhB by 20 %-AgI@$PbBiO_2Br$.

The impact of charge transfer and separation on the photocatalytic efficacy of materials was methodically assessed through PL and EIS analyses. PL spectroscopy functions as a precise method to examine the recombination dynamics of photoinduced charge carriers. A diminished PL intensity typically indicates a reduction in the recombination of photoinduced electron–hole pairs, subsequently increasing the availability of charge carriers for redox reactions and thereby enhancing photocatalytic efficiency. Fig. 15a demonstrates that the PL emission intensity of the 20 %-AgI@$PbBiO_2Br$ composite is markedly inferior to that of pure $PbBiO_2Br$. The decrease in PL intensity indicates that the incorporation of AgI significantly inhibits charge carrier recombination, likely due to the establishment of a heterojunction that promotes directional charge transfer and spatial segregation of electrons and holes. Alongside PL analysis, EIS measurements yield important findings into the interface charge transfer behavior of photocatalysts. A reduced arc radius in the Nyquist plot signifies diminished charge transfer resistance, which correlates with enhanced electron transport and superior charge carrier separation at the interface. Fig. 15b illustrates that the Nyquist plot of the 20 %-AgI@$PbBiO_2Br$ composite displays a markedly diminished semicircle diameter in comparison to the pure $PbBiO_2Br$, indicating improved charge transfer kinetics and enhanced conductivity. The improvement is due to the creation of a compatible heterojunction between AgI and $PbBiO_2Br$, which enables the effective migration of photoexcited electrons and holes while reducing their recombination. Thus, the combined PL and EIS results are strong evidence for the improved photoelectric properties of the modified photocatalyst systems. In particular, to achieve high photocatalytic activity, the 20 %-AgI@$PbBiO_2Br$ composite exhibits superior charge carrier dynamics. These results show that the formation of heterojunctions increases photocatalytic efficiency by promoting charge separation and charge transfer.

The suggested photocatalytic pathway for the breakdown of organic contaminants using the AgI@$PbBiO_2Br$ composite is depicted in Fig. 16, based on the aforementioned experimental results. $PbBiO_2Br$ has CB and VB values of −0.88 eV and 1.67 eV, respectively, whereas AgI has CB and VB values of −2.46 eV and 0.32 eV, respectively. Two potential charge transfer mechanisms can be evaluated. In a type-II heterojunction, upon exposure to visible light, both AgI and $PbBiO_2Br$ are activated to produce photogenerated electrons (e^-) and holes (h^+). The photogenerated e^- from the CB of AgI migrate to the CB of $PbBiO_2Br$, and the h^+ from the VB of $PbBiO_2Br$ to the VB of AgI. In comparison to the standard potential of O_2/•O_2^-, the CB of $PbBiO_2Br$ is substantially more negative [66], allowing the e^- accumulated in the CB of $PbBiO_2Br$ to engage with O_2 in the solution and generate •O_2^- radicals. The accumulated h^+ in the VB of AgI lacks the appropriate potential to oxidize H_2O/OH^- into •OH radicals [67], and the e^- in $PbBiO_2Br$ provides only moderate reducing capability. Thus, a type-II pathway fails to elucidate the production of •OH radicals identified by ESR.

Conversely, a Z-scheme heterojunction offers a more precise elucidation. In this system, photoexcited e^- in the CB of $PbBiO_2Br$ recombines with h^+ in the VB of AgI at the interface, leading to the highly reductive e^- in the CB of AgI and the strongly oxidative h^+ in the VB of $PbBiO_2Br$. The e^- in the CB of AgI can combine with aqueous O_2 to generate •O_2^- radicals, which can subsequently undergo a series of reactions (e.g., disproportionation to H_2O_2 followed by photoreduction) to generate •OH radicals, consistent with the ESR data. Meanwhile, the h^+ in the VB of $PbBiO_2Br$ can directly oxidize organic contaminants into non-toxic products, as also reported in previous studies [68,69].

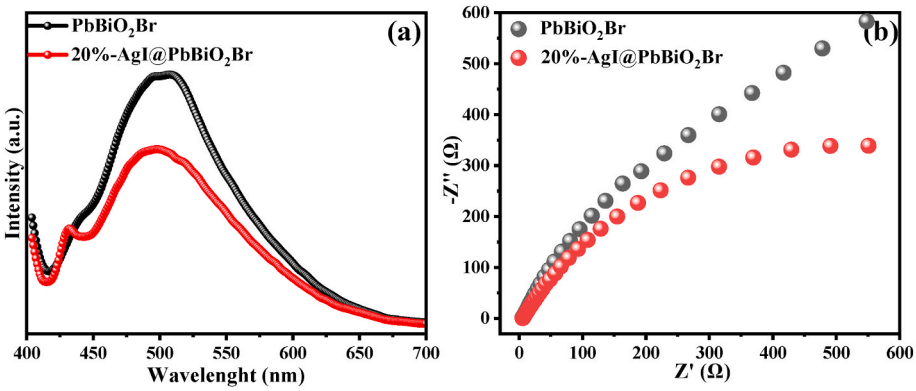

Fig. 15. (a) PL and (b) EIS spectra of the $PbBiO_2Br$ and 20 %-AgI@$PbBiO_2Br$.

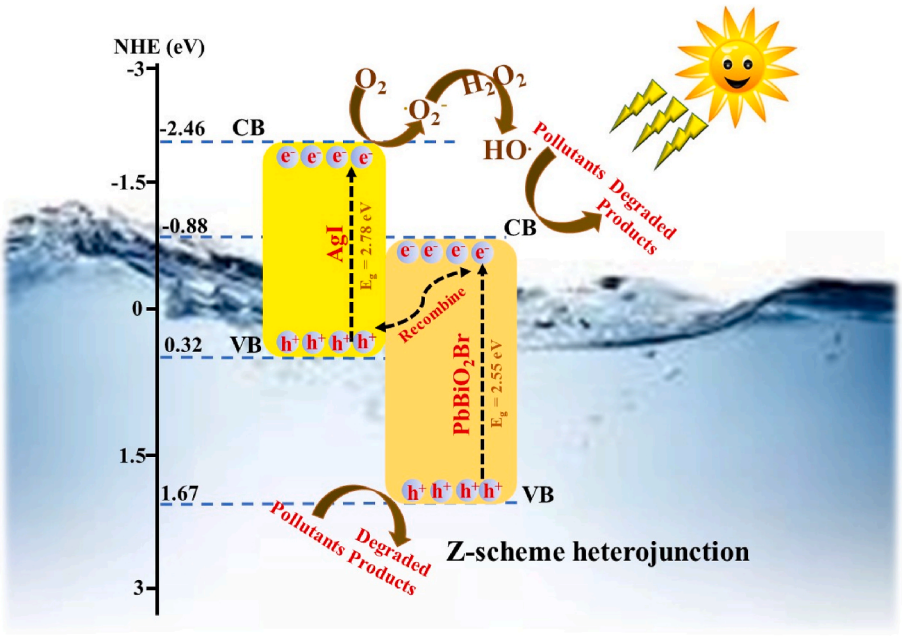

Fig. 16. The possible photodegradation mechanism of the AgI@$PbBiO_2Br$ heterojunction.

Therefore, it can be concluded that the effective formation of Z-scheme heterojunctions between AgI and $PbBiO_2Br$ enhances visible light absorption, boosts efficient charge carrier transport and segregation, and offers exceptional e^- and h^+ oxidation and reduction capabilities.

4. Conclusion

In this study, novel Z-scheme AgI@$PbBiO_2Br$ heterojunctions were successfully fabricated by a facile in situ precipitation process. The fabricated material showed efficient degradation of the organic contaminants and significant antibacterial efficacy against Escherichia coli (E. coli) and Staphylococcus aureus (S. aureus) under visible light exposure. The 20 %-AgI@$PbBiO_2Br$ composite achieved an impressive RhB degradation of 98.72 % within 70 min of visible light exposure compared to pure $PbBiO_2Br$ and AgI. The degradation of methyl orange (MO), neutral red (NR) and tetracycline (TC) by 20 %-AgI@$PbBiO_2Br$ was also investigated, and the nearly total removal of MO, NR, and TC was achieved, respectively. Moreover, the antibacterial efficacy of 20 %-AgI@$PbBiO_2Br$ against E. coli and S. aureus each reaches around 99.99 %. The increased degradation activity is due to the creation of a heterojunction between AgI and $PbBiO_2Br$, which increases effective charge separation and visible light absorption, thus enabling the decomposition of pollutants. Cycling studies confirmed the stability and reusability and showed remarkable photocatalytic durability. The photocatalytic mechanism was investigated in detail using reactive species trapping assays and ESR analysis, and it was found that h^+ and $\bullet O_2^-$ radicals are essential for the photocatalytic process. Additionally, the susceptible active sites of RhB and its potential elimination routes were elucidated by DFT calculations and LC-MS. This research proposes a viable scheme for the production of effective photocatalysts for the elimination of organic contaminants and pathogens from wastewater.

CRediT authorship contribution statement

Ahsan Nazir: Writing – original draft, Software, Investigation, Formal analysis, Data curation, Conceptualization. **Ameena Tur Rasool:** Writing – review & editing, Investigation, Formal analysis. **Chuntao Chen:** Writing – review & editing. **Otabek Mukhitdinov:** Visualization, Data curation. **Doniyor Jumanazarov:** Software, Formal analysis. **Dongping Sun:** Writing – review & editing, Supervision, Project administration, Funding acquisition.

Declaration of competing interest

The authors declare that they have no known competing financial interests or personal relationships that could have appeared to influence the work reported in this paper.

Acknowledgments

This research was supported by the National Natural Science Foundation of China (No. 51803092, 51873087).

Appendix A. Supplementary data

Supplementary data to this article can be found online at https://doi.org/10.1016/j.mssp.2025.110128.

Data availability

Data will be made available on request.

References

[1] A. Nazir, P. Huo, H. Wang, Z. Weiqiang, Y. Wan, A review on plasmonic-based heterojunction photocatalysts for degradation of organic pollutants in wastewater, J. Mater. Sci. 58 (2023) 6474–6515.
[2] A. Nazir, P. Huo, A.T. Rasool, Recent advances on graphitic carbon nitride-based S-scheme photocatalysts: synthesis, environmental applications, and challenges, J. Organomet. Chem. 1004 (2024) 122951.
[3] E.O. Alegbe, T.O. Uthman, A review of history, properties, classification, applications and challenges of natural and synthetic dyes, Heliyon 10 (2024) e33646.
[4] G.A. Ashraf, S. Al-Sulaimi, N. Hassan, Z. Ajmal, F. Atamurotov, R.T. Rasool, M. T. Anwar, N. Husnain, N.H. Alotaibi, H.Y. Alsoqair, Mesoporous Carbon@ZnCuFeS nanoparticles for photocatalytic degradation of organic pollutants via peroxymonosulfate activation, J. Organomet. Chem. 1032 (2025) 123624.
[5] L. Liang, L. Cheng, Y. Zhang, Q. Wang, Q. Wu, Y. Xue, X. Meng, Efficiency and mechanisms of rhodamine B degradation in Fenton-like systems based on zero-valent iron, RSC Adv. 10 (2020) 28509–28515.
[6] M.H. Ashfaq, M. Imran, A. Haider, A. Shahzadi, M. Mustajab, A. Ul-Hamid, W. Nabgan, F. Medina, M. Ikram, Antimicrobial potential and rhodamine B dye degradation using graphitic carbon nitride and polyvinylpyrrolidone doped bismuth tungstate supported with in silico molecular docking studies, Sci. Rep. 13 (2023) 17847.

[7] S. Aguilar, B. Guerrero, Á. Benítez, D.R. Ramos, J.A. Santaballa, M. Canle, D. Rosado, J. Moreno-Andrés, Inactivation of E. coli and S. aureus by novel binary clay/semiconductor photocatalytic macrocomposites under UVA and sunlight irradiation, J. Environ. Chem. Eng. 11 (2023) 110813.

[8] L. Zhang, Y. Jin, L. Xue, H. Zhang, N. Yang, X. Xu, Inactivation effects on escherichia coli in selected liquid food models by induced electric field: germicidal efficacy and putative mechanism, Food Bioprocess Technol. 18 (2025) 7943–7955.

[9] M. Santosham, A. Chandran, S. Fitzwater, C. Fischer-Walker, A.H. Baqui, R. Black, Progress and barriers for the control of diarrhoeal disease, Lancet 376 (2010) 63–67.

[10] Y. Li, J. Bu, Y. Sun, Z. Huang, X. Zhu, S. Li, P. Chen, Y. Tang, G. He, S. Zhong, Efficient degradation of norfloxacin by synergistic activation of PMS with a three-dimensional electrocatalytic system based on Cu-MOF, Sep. Purif. Technol. 356 (2025) 129945.

[11] J.Y. Lu, Z.Q. Bu, Y.Q. Lei, D. Wang, B. He, J. Wang, W.T. Huang, Facile microwave-assisted synthesis of Sb_2O3-CuO nanocomposites for catalytic degradation of p-nitrophenol, J. Mol. Liq. 409 (2024) 125503.

[12] J. Yuennan, S. Al-Sulaimi, M. Karimov, A. Abduvokhidov, M. Mirzayev, G. A. Ashraf, Z. Javed, A. Ayari-Akkari, R.M. Ali, A. Guesmi, P. Channuie, Photocatalytic degradation of tetracycline via peroxymonosulfate activation via $W_{0.5}Ag_{0.5}FeO_3$: a synergistic approach for sustainable water treatment, Vacuum 241 (2025) 114639.

[13] M. Boujelbene, A.B.M. Ali, K. Alsaikhan, A. BaQais, M.B.B. Hamida, A. Amari, Y. Yusupov, A. Abduvokhidov, E. Khudoynazarov, Enhanced photocatalytic performance for organic pollutants degradation and H_2O_2 production using a novel rGO-bridged Bi_2MoO_6-$CoTiO_3$ Z-scheme composites: analytical characterization, mechanism and toxicity assessment, Surf. Interfaces 72 (2025) 107201.

[14] J. Iyyappan, B. Gaddala, R. Gnanasekaran, M. Gopinath, D. Yuvaraj, V. Kumar, Critical review on wastewater treatment using photo catalytic advanced oxidation process: role of photocatalytic materials, reactor design and kinetics, Case Stud. Chem. Environ. Eng. 9 (2024) 100599.

[15] Z. Qi, Z. An, B. Huang, M. Wu, Q. Wu, D. Jiang, Visible-light-catalyzed synthesis of 1,3-benzoxazines via formal [4 + 2] cycloaddition of oximes with o-hydroxybenzyl alcohols, Org. Biomol. Chem. 21 (2023) 6419–6423.

[16] X. Meng, Z. Zhang, Bismuth-based photocatalytic semiconductors: introduction, challenges and possible approaches, J. Mol. Catal. Chem. 423 (2016) 533–549.

[17] T. Saison, S. Usanov, C. Chanéac, O. Durupthy, V. Ruaux, L. Mariey, F. Maugé, P. Beaunier, J.-P. Jolivet, Bi_2O_3, $BiVO_4$, and Bi_2WO_6: impact of surface properties on photocatalytic activity under visible light, J. Phys. Chem. C 115 (2011) 5657–5666.

[18] H. Guo, C.G. Niu, X.J. Wen, L. Zhang, C. Liang, X.G. Zhang, D.L. Guan, N. Tang, G. M. Zeng, Construction of highly efficient and stable ternary AgBr/Ag/$PbBiO_2Br$ Z-scheme photocatalyst under visible light irradiation: performance and mechanism insight, J. Colloid Interface Sci. 513 (2018) 852–865.

[19] Z. He, J. Su, R. Chen, B. Tang, Fabrication of novel p-Ag_2O/n-$PbBiO_2Br$ heterojunction photocatalysts with enhanced photocatalytic performance under visible-light irradiation, J. Mater. Sci. Mater. Electron. 30 (2019) 20870–20880.

[20] B. Wang, J. Di, P. Zhang, J. Xia, S. Dai, H. Li, Ionic liquid-induced strategy for porous perovskite-like $PbBiO_2Br$ photocatalysts with enhanced photocatalytic activity and mechanism insight, Appl. Catal. B Environ. 206 (2017) 127–135.

[21] F.Y. Xiao, J. Xing, L. Wu, Z.P. Chen, X.L. Wang, H.G. Yang, Assembly of ultrathin $PbBiO_2Br$ nanosheets with enhanced visible light photocatalytic properties, RSC Adv. 3 (2013) 10687–10690.

[22] Y. Xia, Z. He, J. Su, S. Zhu, B. Tang, Sustainable solar-light-driven $SrTiO_3$/$PbBiO_2Br$ nanocomposites with enhanced photocatalytic activity, J. Electron. Mater. 49 (2020) 3259–3268.

[23] S. Yuan, X. Liang, Y. Zheng, Y. Chu, X. Ren, Z. Zeng, G. Nan, Y. Wu, Y. He, Enhanced piezocatalytic and piezo-photocatalytic dye degradation via S-scheme mechanism with photodeposited nickel oxide nanoparticles on $PbBiO_2Br$ nanosheets, J. Colloid Interface Sci. 670 (2024) 373–384.

[24] S. Li, X. Wang, Y. Xu, H. Yang, F. Wei, X. Liu, The excellent photocatalytic synergism of $PbBiO_2Br$/UiO-66-NH_2 composites via multiple coupling effects, RSC Adv. 6 (2016) 89907–89915.

[25] Y. Xia, Z. He, J. Su, One-step construction of novel Ag_3PO_4/$PbBiO_2Br$ composite with enhanced photocatalytic activity, Mater. Res. Express 6 (2019) 085909.

[26] Y. Xia, Z. He, J. Su, X. Li, B. Tang, One-step construction of novel $PbBiO_2Br$/ZnO heterojunction composites with enhanced photocatalytic activity, Phys. Status Solidi 216 (2019) 1900406.

[27] Y. Xia, Z. He, J. Su, K. Hu, Construction of novel Cu_2O/$PbBiO_2Br$ composites with enhanced photocatalytic activity, J. Mater. Sci. Mater. Electron. 30 (2019) 9843–9854.

[28] N. Wang, Y. Xing, S. Song, J. Liu, H. Xia, F. Tian, G. Xu, Z. Ren, P. Chen, The synthesis of Ag/AgI with controllable size and silver content via a bola-type assisted protocol and their enhanced photocatalytic performance, Appl. Surf. Sci. 654 (2024) 159521.

[29] P. Thakur, P. Raizada, P. Singh, A. Kumar, A.A.P. Khan, A.M. Asiri, Exploring recent advances in silver halides and graphitic carbon nitride-based photocatalyst for energy and environmental applications, Arab. J. Chem. 13 (2020) 8271–8300.

[30] S. Velmurugan, S. Balu, S. Palanisamy, T.C.K. Yang, V. Velusamy, S.W. Chen, E.S. I. El Shafey, Synthesis of novel and environmental sustainable AgI-Ag_2S nanospheres impregnated g-C_3N_4 photocatalyst for efficient degradation of aqueous pollutants, Appl. Surf. Sci. 500 (2020) 143991.

[31] D.L. Guan, C.G. Niu, X.J. Wen, H. Guo, C.H. Deng, G.M. Zeng, Enhanced Escherichia coli inactivation and oxytetracycline hydrochloride degradation by a Z-scheme silver iodide decorated bismuth vanadate nanocomposite under visible light irradiation, J. Colloid Interface Sci. 512 (2018) 272–281.

[32] F. Chen, Q. Yang, J. Sun, F. Yao, S. Wang, Y. Wang, X. Wang, X. Li, C. Niu, D. Wang, G. Zeng, Enhanced photocatalytic degradation of tetracycline by AgI/$BiVO_4$ heterojunction under visible-light irradiation: mineralization efficiency and mechanism, ACS Appl. Mater. Interfaces 8 (2016) 32887–32900.

[33] I. Ahmad, M. Muneer, A.S. Khder, S.A. Ahmed, Novel type-II heterojunction binary composite (CdS/AgI) with outstanding visible light-driven photocatalytic performances toward methyl orange and tetracycline hydrochloride, ACS Omega 8 (2023) 22708–22720.

[34] M. Ma, H. Sun, X. Yu, C. Xin, J. Liu, J. Guo, M. Li, Y. Tian, Designing step-scheme AgI decorated Ta_2O_{5-x} heterojunctions for boosted photodegradation of organic pollutants, Chemosphere 350 (2024) 141020.

[35] A. Nazir, A.T. Rasool, C. Chen, B. Sun, D. Sun, Rational design and improved visible-light-driven photocatalytic efficacy of NiO-$PbBiO_2Br$ p-n heterojunction for degrading tetracycline in wastewater: DFT simulation and mechanism insight, Mater. Sci. Semicond. Process. 188 (2025) 109265.

[36] X. Duan, Y. Huang, C. Shen, P. Jones, X. Deng, Study on the sterilization performance of photocatalysts used in indoor air purification, Indoor Air 2025 (2025) 1071778.

[37] F. Pan, H. Ji, P. Du, T. Huang, C. Wang, W. Liu, Insights into catalytic activation of peroxymonosulfate for carbamazepine degradation by MnO_2 nanoparticles in-situ anchored titanate nanotubes: mechanism, ecotoxicity and DFT study, J. Hazard Mater. 402 (2021) 123779.

[38] A. Nazir, A.T. Rasool, P. Huo, M.S. Jagirani, Facile fabrication of plasmonic p-n heterojunction Ag@Ag_2O-$PbBiO_2Br$ photocatalyst for levofloxacin and tetracycline degradation: active free radicals for degraded mechanism insight, J. Water Proc. Eng. 59 (2024) 105033.

[39] H. Huang, N. Huang, Z. Wang, G. Xia, M. Chen, L. He, Z. Tong, C. Ren, Room-temperature synthesis of carnation-like ZnO@AgI hierarchical nanostructures assembled by AgI nanoparticles-decorated ZnO nanosheets with enhanced visible light photocatalytic activity, J. Colloid Interface Sci. 502 (2017) 77–88.

[40] N. Ahmad, A.M. Alshehri, Z.R. Khan, I. Ahmad, P.M.Z. Hasan, A.A. Melaibari, M. Shkir, Tailoring of band gap, dielectric and antimicrobial properties of silver iodide nanoparticles through Cu doping, Mater. Sci. Semicond. Process. 137 (2022) 106239.

[41] H. Wang, X. Yuan, Y. Wu, G. Zeng, W. Tu, C. Sheng, Y. Deng, F. Chen, J.W. Chew, Plasmonic Bi nanoparticles and BiOCl sheets as cocatalyst deposited on perovskite-type $ZnSn(OH)_6$ microparticle with facet-oriented polyhedron for improved visible-light-driven photocatalysis, Appl. Catal. B Environ. 209 (2017) 543–553.

[42] H. Guo, C.G. Niu, D.W. Huang, N. Tang, C. Liang, L. Zhang, X.J. Wen, Y. Yang, W. J. Wang, G.M. Zeng, Integrating the plasmonic effect and p-n heterojunction into a novel Ag/Ag_2O/$PbBiO_2Br$ photocatalyst: broadened light absorption and accelerated charge separation co-mediated highly efficient visible/NIR light photocatalysis, Chem. Eng. J. 360 (2019) 349–363.

[43] X.J. Wen, C.G. Niu, L. Zhang, C. Liang, H. Guo, G.M. Zeng, Photocatalytic degradation of ciprofloxacin by a novel Z-scheme CeO_2–Ag/AgBr photocatalyst: influencing factors, possible degradation pathways, and mechanism insight, J. Catal. 358 (2018) 141–154.

[44] Y. Peng, H. Zhou, Y. Wu, Z. Ma, R. Zhang, H. Tu, L. Jiang, A new strategy to construct cellulose-chitosan films supporting Ag/Ag_2O/ZnO heterostructures for high photocatalytic and antibacterial performance, J. Colloid Interface Sci. 609 (2022) 188–199.

[45] M. Yang, K. Zhou, Synthesis and characterizations of spherical hollow composed of AgI nanoparticle using AgBr as the precursor, Appl. Surf. Sci. 257 (2011) 2503–2507.

[46] Q. Guo, X. Wang, P. Zhao, Z. Zhang, L. Geng, Y. Liu, Y. Teng, Y. Zhong, L. Kang, Performance enhancement of carbon nanotube network transistors via SbI_3 inner-doping in selected regions, Adv. Mater. 37 (2025) 2415442.

[47] M. Xu, J. Yang, C. Sun, Y. Cui, L. Liu, H. Zhao, B. Liang, Facile assembly of $BiVO_4$/protonated g-C_3N_4/AgI with a novel dual Z-scheme mechanism for visible-light photocatalytic degradation of Rhodamine B, J. Mater. Sci. 56 (2021) 1328–1346.

[48] A.T. Rasool, A. Nazir, Q. Zhang, E. Li, Fabrication of novel TiN@Cu_2O nanocomposite for efficient photodegradation of sulfamethoxazole by peroxymonosulfate stimulation and bacterial inactivation: DFT analysis and mechanism insight, J. Environ. Chem. Eng. 13 (2025) 117750.

[49] J. Pan, Z. He, J. Su, R. Chen, B. Tang, Preparation and optical properties of Ni-doped $PbBiO_2Br$ nanoparticles, Mater. Res. Express 6 (2019) 115042.

[50] J. Hasan, G. Ouyang, J. Wang, H. Li, G. Tian, C. Qin, Efficient visible-light-driven photocatalysis of flower-like composites of AgI nanoparticle dotting BiOI nanosheet, J. Solid State Chem. 297 (2021) 122044.

[51] J. Ma, L. Shi, L. Yao, Z. Wang, C. Lu, W. Qi, D. Su, AgI nanoparticles evenly dispersed on 2D porous Bi_5O_7I sheets: simple synthesis and excellent photocatalytic performance, ChemistrySelect 2 (2017) 8535–8540.

[52] R.U. Rasool, S. Al-Sulaimi, J. Yuennan, G.A. Ashraf, M. Mirzayev, F. Atamurotov, A. Abdujabbarov, A. Ayari-Akkari, P. Channuie, R. Zhang, Dual-purpose Z-scheme $CsPbBr_3$/ZnS/CeO_2 nanocomposites for PMS activation and photocatalytic hydrogen generation, Mater. Sci. Semicond. Process. 200 (2025) 109890.

[53] S.K. Lakhera, R. Venkataramana, G. Mathew, H.Y. Hafeez, B. Neppolian, Fabrication of high surface area AgI incorporated porous $BiVO_4$ heterojunction photocatalysts, Mater. Sci. Semicond. Process. 106 (2020) 104756.

[54] L. Yang, M. Gao, B. Dai, X. Guo, Z. Liu, B. Peng, Synthesis of spindle-shaped AgI/TiO_2 nanoparticles with enhanced photocatalytic performance, Appl. Surf. Sci. 386 (2016) 337–344.

[55] W. Xue, Z. Peng, D. Huang, G. Zeng, X. Wen, R. Deng, Y. Yang, X. Yan, In situ synthesis of visible-light-driven Z-scheme AgI/Bi_2WO_6 heterojunction photocatalysts with enhanced photocatalytic activity, Ceram. Int. 45 (2019) 6340–6349.

[56] G. Li, L. Peng, B. Wu, Z. Xi, A. Kushwaha, D. Srivastava, A. Kumar, M. Muddassir, J.-C. Jin, A new 3D Zn-based MOF with enhanced UV-light promoted photocatalytic activity for dye degradation, J. Mol. Struct. 1294 (2023) 136417.
[57] J. Huang, G. Nie, Y. Ding, Metal-free enhanced photocatalytic activation of dioxygen by g-C_3N_4 doped with abundant oxygen-containing functional groups for selective N-deethylation of rhodamine B, Catalysts 10 (2020) 6.
[58] X. Yan, T. Ohno, K. Nishijima, R. Abe, B. Ohtani, Is methylene blue an appropriate substrate for a photocatalytic activity test? A study with visible-light responsive titania, Chem. Phys. Lett. 429 (2006) 606–610.
[59] F.R. Amalia, M. Takashima, B. Ohtani, Are you still using organic dyes? Colorimetric formaldehyde analysis for true photocatalytic-activity evaluation, Chem. Commun. 58 (2022) 11721–11724.
[60] Y.E. Ouardi, A.E. Aissouq, A. Chennah, A. Ouammou, K. Laatikainen, Synthesis, characterization, and DFT investigation of rhodamine B dye removal by activated carbon produced from argan nutshell, Biomass Convers. Biorefin. 14 (2024) 15107–15118.
[61] Y.B. Shankar Rao, M.V.S. Prasad, N. Udaya Sri, V. Veeraiah, Vibrational (FT-IR, FT-Raman) and UV–Visible spectroscopic studies, HOMO–LUMO, NBO, NLO and MEP analysis of Benzyl (imino (1H-pyrazol-1-yl) methyl) carbamate using DFT calculations, J. Mol. Struct. 1108 (2016) 567–582.
[62] G.A. Ashraf, R.T. Rasool, M. Pasha, R.U. Rasool, J. Chen, A.A. Khosa, S. Mahmood, M. Hassan, H. Guo, Peroxymonosulfate-based photocatalytic oxidation of tetracycline by $Fe_2(MoO_4)_3/Cd_{0.5}Ni_{0.5}$ S heterostructure; DFT simulation, Chemosphere 309 (2022) 136423.
[63] H. Shi, Y. Xie, W. Wang, L. Zhang, X. Zhang, Y. Shi, J. Fan, Z. Tang, In-situ construction of step-scheme $MoS_2/Bi_4O_5Br_2$ heterojunction with improved photocatalytic activity of Rhodamine B degradation and disinfection, J. Colloid Interface Sci. 623 (2022) 500–512.
[64] Y. Yang, M. Xu, L. Ai, N. Guo, C. Leng, C. Tan, M. Lu, L. Wang, L. Huang, D. Jia, In situ growth of flower sphere Bi_2WO_6/Bi-MOF heterojunction with enhanced photocatalytic degradation of pollutants: DFT calculation and mechanism, J. Environ. Chem. Eng. 11 (2023) 109873.
[65] Y. Wu, L.H. Kong, R.F. Shen, X.J. Guo, W.T. Ge, W.J. Zhang, Z.Y. Dong, X. Yan, Y. Chen, W.Z. Lang, Highly dispersed and stable Fe species supported on active carbon for enhanced degradation of rhodamine B through peroxymonosulfate activation: mechanism analysis, response surface modeling and kinetic study, J. Environ. Chem. Eng. 10 (2022) 107463.
[66] A.O. Oluwole, T.L. Yusuf, S.M. Tichapondwa, M.O. Daramola, S.A. Iwarere, Enhanced photocatalytic efficiency of a novel GO/Bi_2SO_5/AgBr ternary heterojunction for the degradation of tetracycline and rhodamine B, J. Environ. Chem. Eng. 13 (2025) 116777.
[67] S. Ji, J. Dong, M. Ji, W. Zou, S. Yin, Z. Chen, J. Xia, Rapid dual-channel electrons transfer via synergistic effect of LSPR effect and build-in electric field in Z-scheme $W_{18}O4_9$/BiOBr heterojunction for organic pollutants degradation, Inorg. Chem. Commun. 138 (2022) 109283.
[68] R.T. Rasool, G.A. Ashraf, M. Pasha, M.F. Saleem, D. Ghernaout, M.M. Fadhali, H. Guo, Nanoscaled $MnSnO_2$@$CsPbBr_3$ quantum dots heterostructure photocatalyst as efficient organic pollutants degradation by peroxymonosulfate; DFT calculation, J. Mater. Sci. Technol. 153 (2023) 41–55.
[69] X. Wu, Y. Tang, F. Chen, W. Sun, Z. Zhu, J. Zhang, Fabrication and photocatalytic properties of a novel Z-scheme heterojunction ZIF-67/SnS_2, J. Phys. Chem. Solid. 192 (2024) 112100.